

# La<sub>2</sub>O<sub>3</sub>/Fe<sub>2</sub>O<sub>3</sub>-CeO<sub>2</sub> Composite Oxide Catalyst and Its Performance

Youfeng Li\*, Jinliang Lin, Guangwei Wang

School of Chemistry and Chemical Engineering, Zunyi Normal College, Zunyi, China

Email: \*490742310@qq.com

**How to cite this paper:** Li, Y.F., Lin, J.L. and Wang, G.G. (2019) La<sub>2</sub>O<sub>3</sub>/Fe<sub>2</sub>O<sub>3</sub>-CeO<sub>2</sub> Composite Oxide Catalyst and Its Performance. *Advances in Materials Physics and Chemistry*, 9, 219-233.

<https://doi.org/10.4236/ampc.2019.912017>

**Received:** July 24, 2019

**Accepted:** December 8, 2019

**Published:** December 11, 2019

Copyright © 2019 by author(s) and Scientific Research Publishing Inc.

This work is licensed under the Creative Commons Attribution International License (CC BY 4.0).

<http://creativecommons.org/licenses/by/4.0/>



Open Access

## Abstract

The La<sub>2</sub>O<sub>3</sub>/Fe<sub>2</sub>O<sub>3</sub>-CeO<sub>2</sub> composite oxide catalysts were prepared by coprecipitation method, sol-gel method and hydrothermal method. The effect of preparation methods on structure morphology and photocatalytic properties of La<sub>2</sub>O<sub>3</sub>/Fe<sub>2</sub>O<sub>3</sub>-CeO<sub>2</sub> samples was investigated. The results show that the cubic CeO<sub>2</sub> structure can be obtained at 600°C. The rod-shaped sample prepared by coprecipitation method, displays the highest crystalline and the strongest diffraction peak intensity. The spherical sample is acquired from sol-gel method, while the small granular sample prepared by hydrothermal method tends to aggregate. The maximum specific surface area of the sample prepared by coprecipitation method is 76.21 m<sup>2</sup>/g, the minimum specific area of the sample from sol-gel method is 32.66 m<sup>2</sup>/g and the maximum pore size is 13.84 nm, while the minimum pore volume and pore size of the sample by hydrothermal method are 0.038 cm<sup>3</sup>/g and 3.95 nm respectively. The band gap energy of catalyst samples is in the following order: sample-CP < sample-SG < sample-HT. The sample obtained by coprecipitation method has the best catalytic degradation performance for methylene blue. Under the excitation of visible light, the degradation rate was 99.58% at 50 minutes, which was higher than those of sol-gel method and hydrothermal method by 5.58% and 9.54% respectively. The catalytic degradation reaction is a first-order kinetic model:  $\ln(c_0/ct) = kt + q_e$ . The maximum  $k$ -value of the sample degradation process obtained by coprecipitation method is 0.074 min<sup>-1</sup>.

## Keywords

La<sub>2</sub>O<sub>3</sub>/Fe<sub>2</sub>O<sub>3</sub>-CeO<sub>2</sub>, Composite Oxide, Synthetic Method, Catalytic Degradation, Wastewater Treatment

## 1. Introduction

There is about 2.37 billion ton textile wastewater discharged from Chinese textile

industry every year, among which dyeing wastewater accounts for about 80%. The color of dyeing wastewater is particularly serious pollution, and it is difficult to remove by general biochemical methods. The recycling rate of wastewater after treatment in the whole textile industry is only about 10%. Therefore, the treatment and emission reduction of dyeing wastewater are urgent for improving the quality of water environment. Photocatalytic technology is a good application prospect in the fields of environmental purification, solar energy utilization and self-cleaning [1] [2] [3].

CeO<sub>2</sub> has attracted much attention in photocatalytic degradation of wastewater contaminants for its unique crystal structure, high oxygen storage, and oxygen release capacity. The activity and selectivity of pure CeO<sub>2</sub> catalyst generally are improved by adjusting morphology and particle size of CeO<sub>2</sub>, so its catalytic oxidation technology is insufficiently pushed to a wide range of practical applications [4] [5] [6]. Researchers have tried to synthesize multi-component Ce-based composite oxide catalysts by doping transition metal M into CeO<sub>2</sub>. The lattice distortion of CeO<sub>2</sub> results in defects when CeO<sub>2</sub> interacts with transition metal M for its variable valence and excellent redox performance. Then it accelerates the flow of oxygen in the crystal phase and provides more active oxygen species for catalytic oxidation. So the catalytic activity and stability of the Ce-based composite oxide catalysts are greatly improved [7]. Choi *et al.* [8] studied the effect of various metal ions on the photocatalytic activity of titanium dioxide, among which the effect of Fe<sup>3+</sup> was the best. Machida *et al.* [9] found that the oxygen storage/release capacity of CeO<sub>2</sub>-Fe<sub>2</sub>O<sub>3</sub> composites was better than that of pure components CeO<sub>2</sub> and Fe<sub>2</sub>O<sub>3</sub>. They also pointed out that CeO<sub>2</sub> was the entrance of oxygen storage. The high temperature reaction activity and thermal stability of the La modified Ni/CeO<sub>2</sub>-ZrO<sub>2</sub> catalysts were improved because La<sup>3+</sup> doped into Ni/CeO<sub>2</sub>-ZrO<sub>2</sub> oxides could produce more oxygen vacancies during high temperature sintering, and then the oxygen mobility was enhanced [10]. In this paper, Ce-based composite oxide catalysts were prepared with transition metals of Fe<sup>3+</sup> and La<sup>3+</sup> doped into CeO<sub>2</sub>, and their performances were also investigated.

The preparation methods of Ce-based composite oxide catalysts have shown great influence on their structure and morphology. The preparation methods are hydrothermal method [11], sol-gel method [12], combustion method [13], precipitation method [14], template method [15], and so on. In the paper, the La<sub>2</sub>O<sub>3</sub>/Fe<sub>2</sub>O<sub>3</sub>-CeO<sub>2</sub> catalysts with different morphologies were prepared by coprecipitation method, sol-gel method and hydrothermal method. The effects of preparation methods on the structure and performance of the La<sub>2</sub>O<sub>3</sub>/Fe<sub>2</sub>O<sub>3</sub>-CeO<sub>2</sub> catalysts were studied.

## 2. Experimental Sections

### 2.1. Preparation of La<sub>2</sub>O<sub>3</sub>/Fe<sub>2</sub>O<sub>3</sub>-CeO<sub>2</sub> Catalyst

The reagents Ce(NO<sub>3</sub>)<sub>3</sub>·6H<sub>2</sub>O, Fe(NO<sub>3</sub>)<sub>3</sub>·9H<sub>2</sub>O, La(NO<sub>3</sub>)<sub>3</sub>·6H<sub>2</sub>O, polyethyleneg-

lycol (PEG), ammonium bicarbonate, urea, and methylene blue from China National Medicines Corporation Ltd. were analytically pure. All the chemicals were AR grade, and used as received without further purification. Deionized water was used in all experiments.

**Coprecipitation method:** First, 0.868 g  $\text{Ce}(\text{NO}_3)_3 \cdot 6\text{H}_2\text{O}$ , corresponding Stoichiometric ratio  $\text{Fe}(\text{NO}_3)_3 \cdot 9\text{H}_2\text{O}$  and  $\text{La}(\text{NO}_3)_3 \cdot 6\text{H}_2\text{O}$  were dissolved in deionized water, then the solution was added into 250 ml three-port bottle. The polyethylene glycol (PEG) solution was slowly added into the three-port bottle with 0.21 g PEG as complexing agent dissolved in 40 ml water. Then the precipitator  $\text{NH}_4\text{HCO}_3$  was added into to mixed solution to aid precipitate at  $80^\circ\text{C}$  under agitation. After aging at  $100^\circ\text{C}$  for 10 h for 24 h, the precipitate was filtrated and washed with deionized water. The  $\text{La}_2\text{O}_3/\text{Fe}_2\text{O}_3\text{-CeO}_2$  precursor samples were obtained after the precipitate being dried, followed by calcinating in a muffle furnace at  $600^\circ\text{C}$  for 4 h. The corresponding  $\text{La}_2\text{O}_3/\text{Fe}_2\text{O}_3\text{-CeO}_2$  composite sample was denoted as sample-CP.

**Sol-gel method:** First, 0.868 g  $\text{Ce}(\text{NO}_3)_3 \cdot 6\text{H}_2\text{O}$ , corresponding Stoichiometric ratio  $\text{Fe}(\text{NO}_3)_3 \cdot 9\text{H}_2\text{O}$  and  $\text{La}(\text{NO}_3)_3 \cdot 6\text{H}_2\text{O}$  were dissolved in deionized water to obtain mixed solution, then the mixed solution was added into 250 ml three-port bottle. The polyethylene glycol (PEG) solution was slowly added into the three-port bottle with 0.21 g PEG as complexing agent dissolved in 40 ml water. Then the mixed solution was agitated at  $80^\circ\text{C}$  to obtain sol. The scarlet  $\text{La}_2\text{O}_3/\text{Fe}_2\text{O}_3\text{-CeO}_2$  gel precursor was obtained after the sol was dried at  $100^\circ\text{C}$  for 10 h. The  $\text{CeO}_2$  compound oxide samples were acquired by calcinating  $\text{CeO}_2$  gel in a muffle furnace at  $600^\circ\text{C}$  for 4 h. The corresponding  $\text{La}_2\text{O}_3/\text{Fe}_2\text{O}_3\text{-CeO}_2$  composite sample was denoted as sample-SG.

**Hydrothermal method:** First 0.21 g PEG and 1.0 g urea were dissolved in distilled water, and continued stirring to make the mixture solution. Then 0.868 g  $\text{Ce}(\text{NO}_3)_3 \cdot 6\text{H}_2\text{O}$ , corresponding Stoichiometric ratio  $\text{Fe}(\text{NO}_3)_3 \cdot 9\text{H}_2\text{O}$  and  $\text{La}(\text{NO}_3)_3 \cdot 6\text{H}_2\text{O}$  were added into the mixture solution and stirred for 0.5 h at  $80^\circ\text{C}$ . Finally, the mixed solution was transferred to a polytetrafluoroethylene high-pressure hydrothermal kettle of 100 ml for 24 hours at 140 C. The precipitate was filtrated and washed with deionized water. The  $\text{La}_2\text{O}_3/\text{Fe}_2\text{O}_3\text{-CeO}_2$  precursor samples were obtained after the precipitate being dried, followed by drying in oven at 80 C for 10 h then calcinating in a muffle furnace at  $600^\circ\text{C}$  for 4 h. The corresponding  $\text{La}_2\text{O}_3/\text{Fe}_2\text{O}_3\text{-CeO}_2$  composite sample was denoted as sample-HT.

The molar ratio of  $\text{La}^{3+}:\text{Fe}^{3+}$  was 1:2, and the molar doping amount of  $\text{La}_2\text{O}_3$  and  $\text{Fe}_2\text{O}_3$  in  $\text{La}_2\text{O}_3/\text{Fe}_2\text{O}_3\text{-CeO}_2$  was 3% in the experiment.

## 2.2. Catalytic Degradation Experiments

Catalytic degradation experiments were performed in a double beaker of 250 ml with water cooling. A portion of catalyst (10 mg) and  $\text{H}_2\text{O}_2$  (6 ml) were introduced into 100 ml of aqueous dye solution containing methylene blue at a con-

centration of  $100 \text{ mg}\cdot\text{L}^{-1}$ . Sodium hydroxide and hydrochloric acid solution were used to adjust the pH value of the solution. Adsorption equilibrium was attained by the reaction solution after magnetic stirring for 30 min in the dark. The degradation reaction was then performed using 300 W xenon lamps as visible light. Liquid samples were removed at regular 10 min intervals for analysis of the absorbance. To evaluate the catalytic activity of the catalysts, the dye removal efficiency ( $\eta$ ) was calculated, as shown below:

$$\eta = \frac{c_0 - c_t}{c_0} \times 100\%,$$

where  $c_0$  is the initial after the dark equilibrium, and  $c_t$  is different times absorbance values of methylene blue, respectively.

### 2.3. Catalyst Characterization

A thermogravimetric (TG/DSC) analysis was conducted on an STD Q600 instrument at a rate of  $5^\circ\text{C}\cdot\text{min}^{-1}$  under nitrogen protection. The crystalline phases of the as-prepared  $\text{CeO}_2$  composite oxides were studied by x-ray diffraction (XRD) with a Bruker/AXS D8 Advance X-ray diffractometer operated at 40 kV and 200 mA with Cu K $\alpha$  radiation ( $\lambda = 0.15418 \text{ nm}$ ). The morphology and dispersion of the powders were observed with the use of a transmission electron microscope (TEM, JEOL-6360LV). Textural properties of the samples were measured by the Brunauer-Emmett-Teller (BET) model on a Quantachrome NOVA instrument, with Aras the carrier gas and  $\text{N}_2$  as the adsorbent at  $-196^\circ\text{C}$ . The visible light absorbance at the characteristic wavelength of 664 nm for methylene blue dye was measured with a UV-2500 spectrophotometer.

## 3. Results and Discussions

### 3.1. TG/DSC Analysis

**Figure 1** shows the TG/DSC curves of the dried  $\text{La}_2\text{O}_3/\text{Fe}_2\text{O}_3\text{-CeO}_2$  precursors with a heating rate of  $5^\circ\text{C}\cdot\text{min}^{-1}$ . DSC curves display endothermic peaks and exothermic peaks of the dried precursors. The about  $150^\circ\text{C}$  endothermic peak can be explained by the removal of adsorbed water and crystal water. The about  $200^\circ\text{C}$  exothermic peaks can be explained by the burning and decompose of PEG in the precursor powders. Major mass loss of the precursor samples occurs below  $500^\circ\text{C}$ . The overall weight loss is 20% - 50%. The thermal decomposition of precursor from the coprecipitation method was showed in **Figure 1(A)**. The main mass loss occurred below  $300^\circ\text{C}$ . A small endothermic peak at  $150^\circ\text{C}$  could be attributed to the loss of adsorbed water and crystal water, which accounting for about 10% of the total mass loss. There are two exothermic peaks between  $200^\circ\text{C}$  and  $300^\circ\text{C}$ , which were caused by the decomposition of  $\text{Ce}(\text{OH})_3$  and  $\text{Ce}_2(\text{CO}_3)_3$  precursors, accounting for about 40% of the total mass loss. The different interaction between PEG and metal ions leads to varied decomposition temperature. When the temperature is about  $520^\circ\text{C}$ , there is another exothermic

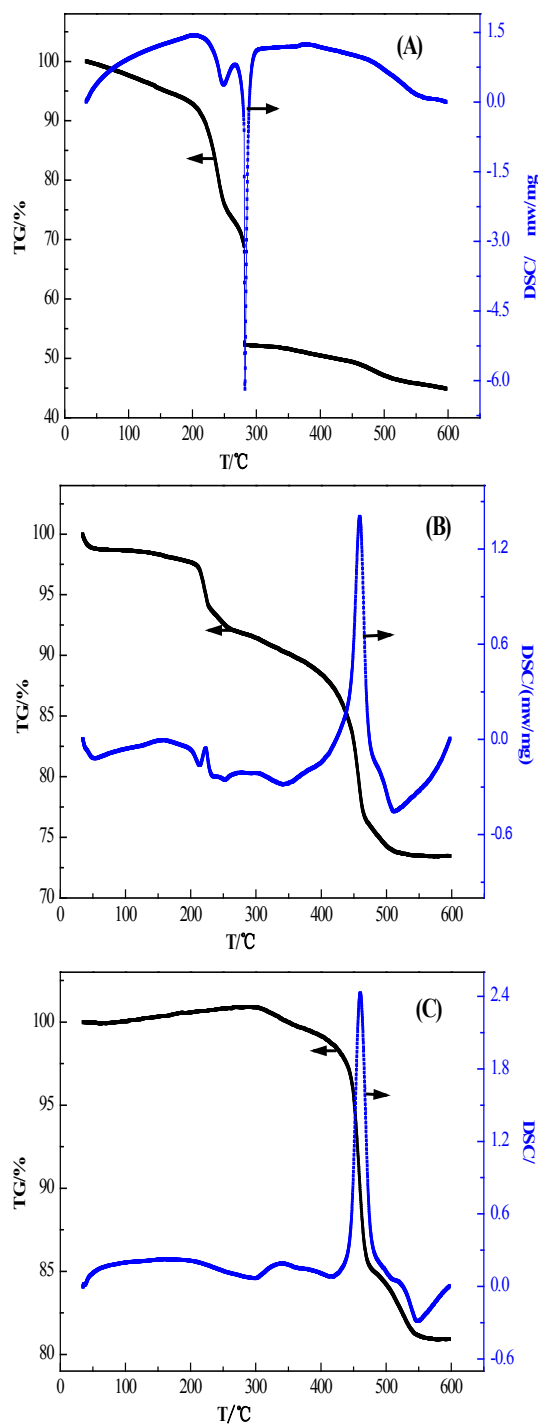


**Figure 1.** TG/DSC curves of precursors synthesized by different methods: (A) CP, (B) SG, (C) HT.

peak which shows crystal formation. The mass loss of precursor samples by co-precipitation method mainly occurs in two regions of 200°C - 250°C and 300°C - 460°C, with a total loss of about 25%. The corresponding exothermic peak at 200°C - 250°C can be attributed to thermal decomposition of residual PEG in precursor sample-SG. The strong endothermic peak at 300°C - 460°C can be

decomposed of PEG additives (shown in **Figure 1(B)**). While at about 350°C - 550°C, there occurs an exothermic peak of sample-HT precursors in the heating process which implies the decomposition of precipitates of precursor  $\text{Ce}(\text{HCOO})_3$  and the formation of  $\text{CeO}_2$  crystal phases, with a total weight loss of about 20% (**Figure 1(C)**). This is proved by the XRD results in **Figure 2**. From the above results, the intermolecular and ionic interactions in the precursor precipitates prepared by different methods are different. So the thermal stability of precursors and the decomposition temperature of samples are different.

### 3.2. XRD Analysis

The XRD patterns of  $\text{La}_2\text{O}_3/\text{Fe}_2\text{O}_3\text{-CeO}_2$  samples are exhibited in **Figure 2**. The peaks around  $2\theta = \sim 28.5^\circ$ ,  $\sim 33.0^\circ$ ,  $\sim 47.5^\circ$ ,  $\sim 57.5^\circ$  and  $\sim 69.5^\circ$  in agreement with the (111), (200), (220), (311) and (400) planes of the cubic fluorite structure of  $\text{CeO}_2$ , respectively. The crystal form is consistent with the standard JCPDS (34-0394) spectra [16]. The results show that the main active component of the catalyst is crystallized  $\text{CeO}_2$  with cubic fluorite structure and this structure remains after calcinating process. However, the crystallinity of the samples varies greatly with different synthesis methods. Sample-CP shows the best crystallinity and strongest diffraction peak intensity. To resume, the crystallinity of catalyst samples is in the following order: sample-CP > sample-SG > sample-HT. According to Scherer formula, the particle sizes of  $\text{La}_2\text{O}_3/\text{Fe}_2\text{O}_3\text{-CeO}_2$  samples prepared by the three methods were calculated to be about 100 nm (sample-CP), 32.56 nm (sample-SG) and 5.23 nm (sample-HT), respectively.

From the diffraction peak in **Figure 2**, we can see that there is no impurity phase peak, and the samples display high purity, while the diffraction peak of the sample obtained by hydrothermal method slightly shifts red. The doping elements La and Fe in the samples are not detected by XRD, indicating that  $\text{La}^{3+}$  and  $\text{Fe}^{3+}$  cations have been well inserted into the  $\text{CeO}_2$  lattice, or  $\text{La}_2\text{O}_3$ -based and  $\text{Fe}_2\text{O}_3$ -based clusters are well dispersed on the surface of  $\text{CeO}_2$  particles [17].

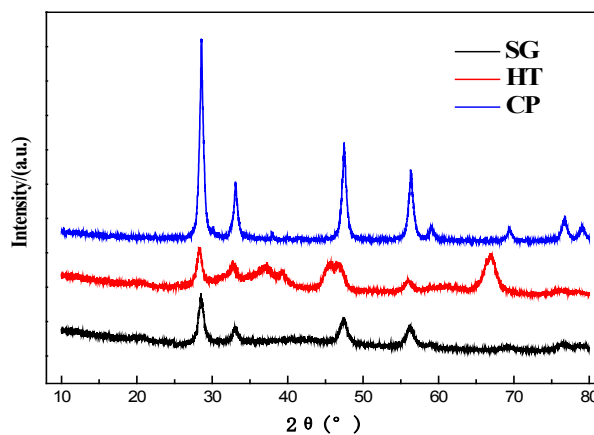


**Figure 2.** XRD of  $\text{La}_2\text{O}_3/\text{Fe}_2\text{O}_3\text{-CeO}_2$  catalysts from different methods.

### 3.3. TEM Analysis

**Figure 3** shows TEM photographs of  $\text{La}_2\text{O}_3/\text{Fe}_2\text{O}_3\text{-CeO}_2$  samples synthesized by different methods. It can be seen that the rod-like sample, with a diameter of about 100 nm, obtained from coprecipitation is well dispersed from **Figure 3(A)**. The sample-SG is spherical and well dispersed, with a diameter of 20 - 40 nm. The samples obtained by hydrothermal method are fine particles, some of which accumulate into electronic clouds. The results consist of the results of XRD. Compared with (A), (B) and (C) in **Figure 3**, it is obvious that the morphologies of samples synthesized by different methods vary greatly.

During the formation of sol-gel, the spherical structure is formed by nanoparticles self-assembly through hydrogen bonds between ethylene glycol molecules. When the gel is dried and calcined at high temperature, the nuclei grow along the isotropic state, and nanospheres are acquired [18]. There are  $\text{Ce}(\text{OH})_3$  and  $\text{Ce}_2(\text{CO}_3)_3$  precipitators formed during coprecipitation. While  $\text{Ce}(\text{OH})_3$  and  $\text{Ce}_2(\text{CO}_3)_3$  are polyhedrons constituted of a series of polyhedrons consisting of  $\text{Ce}^{3+}$  and  $\text{OH}^-$ ,  $\text{CO}_3^{2-}$ . During coprecipitation,  $\text{Ce}^{3+}$  binds with  $\text{OH}^-$  and  $\text{CO}_3^{2-}$  then form nanocrystals with very small size. Nanorods are formed when these nanocrystals grow along the crystal plane with high chemical activity [17].  $\text{Ce-OCH}_2\text{-CH}_2\text{-OH}$  are formed between  $\text{Ce}(\text{HCOO})_3$  and polyethylene glycol in the hydrothermal reaction process, because polyethylene glycol was adsorbed on the positive charge  $\text{Ce}(\text{HCOO})_3$  crystal surface with high chemical activity. Which hindered the growth of  $\text{Ce}(\text{HCOO})_3$  along the crystal surface, resulting in fine nanoparticles. When calcined at high temperature, some of these fine nanoparticles aggregated. The morphology and particle size of  $\text{La}_2\text{O}_3/\text{Fe}_2\text{O}_3\text{-CeO}_2$  samples directly affect their texture properties.

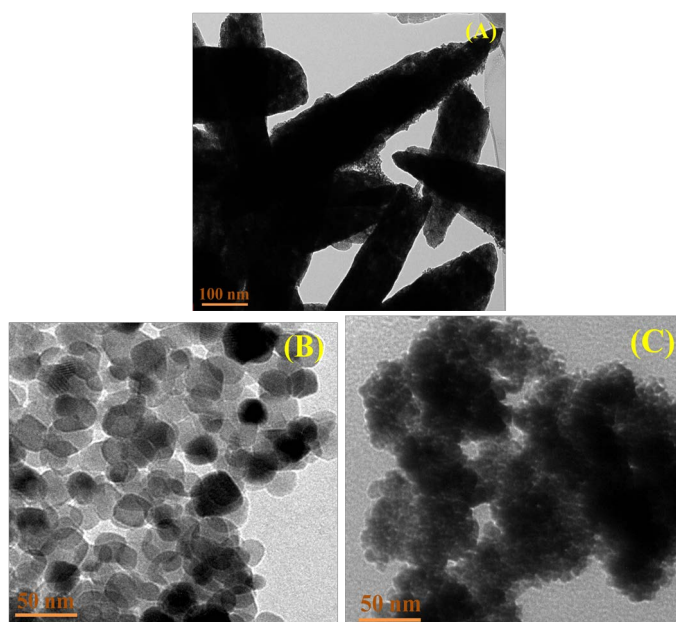


**Figure 3.** TEM photography of  $\text{La}_2\text{O}_3/\text{Fe}_2\text{O}_3\text{-CeO}_2$  catalyst from different methods: (A) CP, (B) SG, (C) HT.

### 3.4. BET Analysis

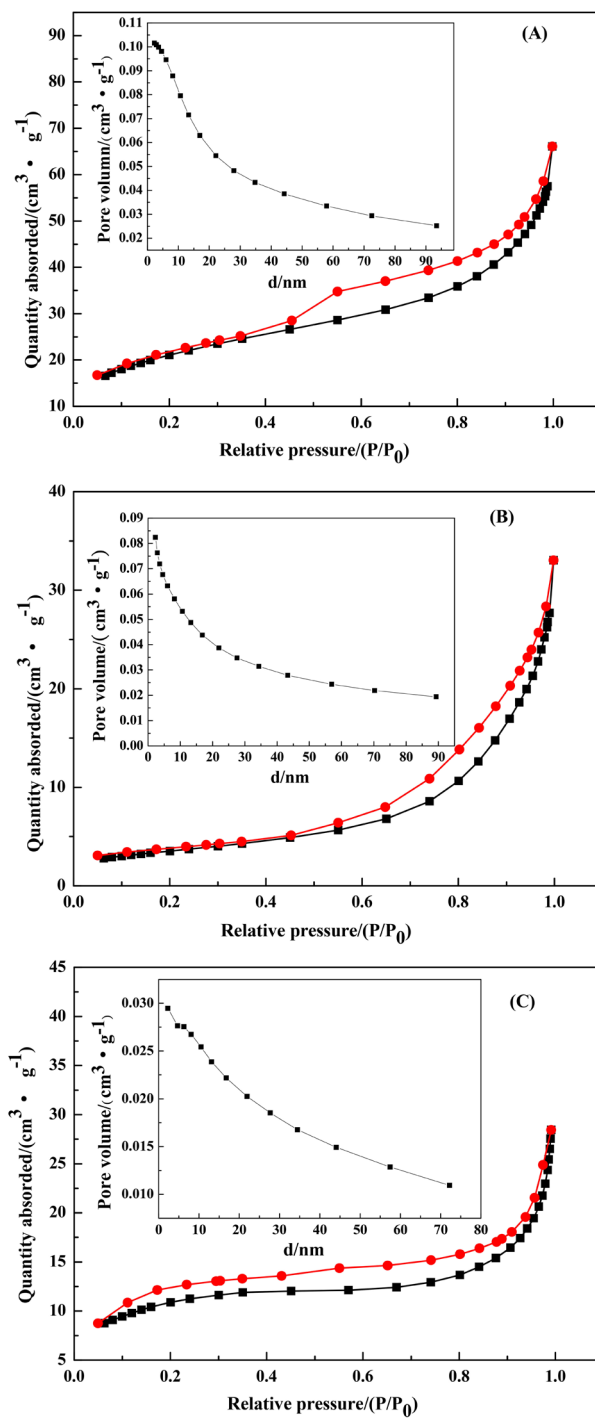
The texture structure of the samples was conducted by N<sub>2</sub> adsorption and desorption method. The specific surface area, pore volume and average pore diameter results of the samples from three methods are shown in **Table 1**. Sample-CP has the highest surface area of 76.21 m<sup>2</sup>·g<sup>-1</sup> and the highest pore volume of 0.091 cm<sup>3</sup>·g<sup>-1</sup>. The smallest surface area of the sample-SG sample are 32.66 m<sup>2</sup>·g<sup>-1</sup>, and the largest pore diameter is 13.84 nm. While the surface area of sample-HT intervene sample-CP and sample-SG, the pore volume and pore diameter were the smallest, the values of them are 53.48 m<sup>2</sup>·g<sup>-1</sup>, 0.038 cm<sup>3</sup>·g<sup>-1</sup> and 3.95 nm, respectively. This may be due to the different decomposition temperature, gas release rate and heat release rate of the precursors during thermal decomposition, which results in obvious difference in pore structure and surface area.

The pore size of the sample-SG shows obvious growth tendency, indicating that the sample-SG possesses better aging resistance and stronger adsorption capacity. During the sol-gel process, the organic dispersant PEG has been kept in the precursor. When calcined at high temperature, PEG decomposes and releases a large amount of gas, resulting in an increase in the pore size of the sample. However, its surface area is the smallest because the particle shape of the sample-SG is spherical. Most PEG is lost following the filtrate during precipitate filtering for coprecipitation process and hydrothermal process. At the same time, the particle size is small and the particles agglomerated seriously of the sample-HT, which reduces the pore volume and pore size. The result is consistent with the thermal analysis results.

**Figure 4** shows the adsorption and desorption isotherms of the La<sub>2</sub>O<sub>3</sub>/Fe<sub>2</sub>O<sub>3</sub>-CeO<sub>2</sub> samples. We can find that three kinds of samples present adsorption and desorption isotherms of mesoporous (2 - 50 nm) materials characteristics. There are also hysteresis loops in the isotherms due to incomplete uniformity of pore shapes and pore size, as well as phenomenon of capillary condensation. Of which, the hysteresis loops of sample-CP are the most obvious, and the hysteresis loops of sample-HT are the smallest. Whatmore, the pore shape of samples is bottle-shaped. Hysteresis loops are formed due to the phenomenon of capillary condensation and incomplete pore size [19]. The adsorption curves of the samples prepared by coprecipitation and sol-gel method increase sharply at the relative pressure ( $P/P_0$ ) of 0.6 - 1.0. It may be due to the larger pore size and relatively concentrated pore size distribution of the sample, and the pore size is mainly concentrated in the mesoporous size. The results are consistent with the pore size distribution curves. It can also be seen from **Figure 4** that among the three samples, desorption of sample-HT is the strongest, and the hysteresis loop formed by adsorption-desorption curve is the most obvious. The adsorption-desorption value of the sample-CP is the largest, followed by the sol-gel method. The value of the hydrothermal method is the smallest, which is consistent with the analysis results of the surface area and pore structure of the La<sub>2</sub>O<sub>3</sub>/Fe<sub>2</sub>O<sub>3</sub>-CeO<sub>2</sub> sample. These textural properties will directly affect the photocatalytic degradation performance of La<sub>2</sub>O<sub>3</sub>/Fe<sub>2</sub>O<sub>3</sub>-CeO<sub>2</sub>.

**Table 1.** Texture properties of different  $\text{La}_2\text{O}_3/\text{Fe}_2\text{O}_3\text{-CeO}_2$  photocatalyst samples.

Sample	$S_{\text{BET}}/(\text{m}^2\cdot\text{g}^{-1})$	$V/(\text{cm}^3\cdot\text{g}^{-1})$	$d_p/(\text{nm})$
Sample-CP	76.21	0.091	4.75
Sample-SG	32.66	0.043	13.84
Sample-HT	53.48	0.038	3.95

**Figure 4.**  $\text{N}_2$  adsorption-desorption isotherms and pore volume distribution of  $\text{La}_2\text{O}_3\text{-Fe}_2\text{O}_3\text{-CeO}_2$  catalyst samples: (A) CP, (B) SG, (C) HT.

### 3.5. La<sub>2</sub>O<sub>3</sub>-Fe<sub>2</sub>O<sub>3</sub>-CeO<sub>2</sub> Photocatalytic Degradation Analysis

**Figure 5** shows the time dependence of the methylene blue removal efficiency by different La<sub>2</sub>O<sub>3</sub>/Fe<sub>2</sub>O<sub>3</sub>-CeO<sub>2</sub> catalysts under 300 W Xenon lamps. The methylene blue removal efficiencies are shown in **Figure 5** for a degradation process with a catalyst concentration of 100 mg·L<sup>-1</sup> at solution pH = 10.0. The sample-CP catalyst shows the best catalytic activity during the catalytic degradation process. The degradation of methylene blue is almost complete at 50 min for La<sub>2</sub>O<sub>3</sub>/Fe<sub>2</sub>O<sub>3</sub>-CeO<sub>2</sub>/γ-Al<sub>2</sub>O<sub>3</sub>, which represents an increase of 5.58% and 9.54%, compared with the efficiencies of sample-SG and sample-HT under the same reaction conditions, respectively. The removal efficiency of methylene blue by sample-CP achieves a maximum value of 99.58% at 50 min. The high catalytic activity is attributed to the texture and morphology of the catalyst sample.

The sample-CP has good adsorption and more active sites on surface for its large surface area. So the catalytic reaction effect is better than the other two. This indicates that catalytic oxidation process is major dependent on adsorption-desorption, and catalytic oxidation also plays an important role. The pore size and pore size of sample-CP are large, which increases the defects inside the lattice and decreases the band gap. It provides more reactive oxygen species for catalytic oxidation and improves the catalytic activity [20]. The sample-HT has small particle size and there is agglomeration among the particles, which leads to the reduction of the catalytic effect.

The degradation reaction of methylene blue can be described by the first-order reaction kinetics:  $\ln(c_0/c_t) = kt + q_e$ , where  $c_0$  and  $c_t$  are the concentration of methylene blue at the initial time and each interval time during irradiation, respectively,  $k$  is the first-order rate constant,  $t$  is the irradiation time and  $q_e$  is a constant. A high  $k$ -value usually implies the fast reaction rate of efficient catalysts [21]. The calculated  $k$  value (in **Figure 6**) is 0.074, 0.063 and 0.060 min<sup>-1</sup> for sample-CP, sample-SG and sample-HT, respectively, which indicates that the sample-CP catalyst exhibits the highest photocatalytic activity. The result is consistent with the results of **Figure 5**.

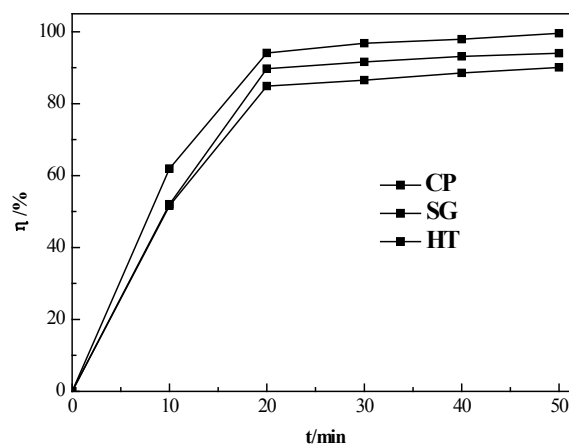


**Figure 5.** Degradation methylene blue results for different La<sub>2</sub>O<sub>3</sub>/Fe<sub>2</sub>O<sub>3</sub>-CeO<sub>2</sub> catalyst samples under Xenon light.

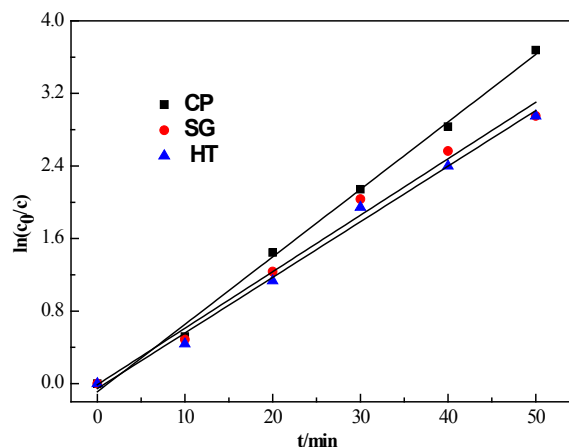


**Figure 6.** Linear fits of  $\ln(c_0/c_t)$  versus time.

### 3.6. Mechanism Analysis

The electron-hole pairs on the surface of the catalyst react with  $\text{H}_2\text{O}$ ,  $\text{H}_2\text{O}_2$  and  $\text{O}_2$ , then form  $\bullet\text{OH}$  and  $\bullet\text{O}_2$ . In the degradation process, methylene blue is first adsorbed on the surface of the catalyst, then reacts with  $\bullet\text{OH}$  and  $\bullet\text{O}_2$  and decomposed into  $\text{CO}_2$  and  $\text{H}_2$  [22]. Researchers found that doped with transition metals, electron-hole pairs on the surface of  $\text{CeO}_2$  will be promoted [23] [24]. When transition metal  $\text{La}^{3+}$  is doped into  $\text{CeO}_2$ , some of  $\text{Ce}^{4+}$  lattices are substituted by  $\text{La}^{3+}$  and produce a large amount of reactive oxygen species, which greatly improves the catalytic activity of  $\text{CeO}_2$  [25]. The doping of  $\text{Fe}^{3+}$  into  $\text{TiO}_2$  results in the decrease of its energy level, catalytic reaction shifted to 400 - 700 nm in the visible region, and the catalytic activity of  $\text{TiO}_2$  catalyst was improved [8]. Therefore, the doping of  $\text{La}^{3+}$  and  $\text{Fe}^{3+}$  into  $\text{CeO}_2$  will result in lattice distortion and defect, decrease energy level, accelerate the flow of oxygen in the crystal phase, and provide more active oxygen species for catalytic oxidation. Therefore, the catalytic activity of  $\text{La}_2\text{O}_3/\text{Fe}_2\text{O}_3\text{-CeO}_2$  samples is enhanced under visible light excitation.

Usually, the visible wavelength is 380 - 760 nm and its corresponding energy is 3.10 - 1.63 eV.  $\text{CeO}_2$  has a large band gap of 3.2 eV, which makes it sensitive to ultraviolet radiation only [23]. The band gap between the valence and conduction bands of the  $\text{CeO}_2$  and  $\text{La}_2\text{O}_3/\text{Fe}_2\text{O}_3\text{-CeO}_2$  samples is determined using UV-vis diffuse reflectance spectra. As shown in **Figure 7(A)**, the large absorption at wavelengths shorter than 400 nm can be attributed to intrinsic band-to-band absorption of  $\text{La}_2\text{O}_3/\text{Fe}_2\text{O}_3\text{-CeO}_2$ . Compared to the  $\text{CeO}_2$ , the  $\text{La}_2\text{O}_3/\text{Fe}_2\text{O}_3\text{-CeO}_2$  compound oxide exhibit significantly increased absorption at above 430 nm, indicating that the loaded  $\text{La}^{3+}$  and  $\text{Fe}^{3+}$  may be helpful for utilizing visible light more effectively. The diffuse reflectance was transferred via Kubelka-Munk function into Tauc plots and the band gap energy of the samples was defined via Tauc plots that are shown in **Figure 7(B)**. The band gap  $\text{La}_2\text{O}_3/\text{Fe}_2\text{O}_3\text{-CeO}_2$  exhibits the energy gaps of sample-CP (2.50 eV), sample-SG (2.68 eV) and sample-HT (2.82 eV) respectively. It is deduced that the decrease

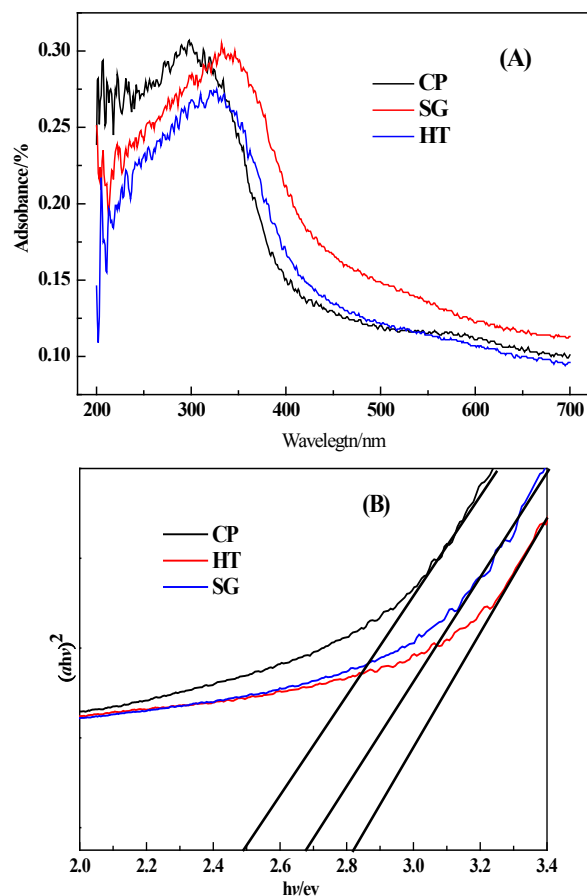


**Figure 7.** UV-Vis diffuse reflectance spectra of different  $\text{La}_2\text{O}_3/\text{Fe}_2\text{O}_3\text{-CeO}_2$  catalyst samples (A);  $(\alpha h\nu)^2$  versus energy ( $h\nu$ ) plots of different  $\text{La}_2\text{O}_3/\text{Fe}_2\text{O}_3\text{-CeO}_2$  catalyst samples (B).

of band gap increases the light absorption, and electrons through absorbing lower photon energy in the valence band more easily jump to the conduction band [24]. Thereby, optical results of  $\text{La}_2\text{O}_3/\text{Fe}_2\text{O}_3\text{-CeO}_2$  imply more efficient processes for visible-light catalytic degradation of methylene blue. Sample-CP shows the best catalytic degradation effect for methylene blue.

#### 4. Conclusion

$\text{La}_2\text{O}_3/\text{Fe}_2\text{O}_3\text{-CeO}_2$  composite oxide catalysts were prepared by coprecipitation method, sol-gel method and hydrothermal method. The catalyst was  $\text{CeO}_2$  phase with cubic fluorite structure. The samples with different morphology were obtained due to varied interaction forces between ions and molecules in the precursors, and different decomposition processes. The rod-shaped sample from coprecipitation method was about 100 nm particles with good dispersivity, 20 - 40 nm spheres sample obtained by sol-gel method, and it was small agglomerated particles by hydrothermal method. The morphology and particle size of the sample directly affected its texture properties of surface area, pore volume and pore diameter. Catalytic degradation performance depends not only on

structure and texture properties, but also on band gap of the catalyst. The catalytic degradation rate of methyl blue under visible light is in the following order: sample-CP > sample-SG > sample-HT.

## Acknowledgements

This project was financially supported by the projects of “Qian Jiao He KY” [2019] 114 and “Talents of Qian Ke He Platform” ([2017]5727-11).

## Conflicts of Interest

The authors declare no conflicts of interest regarding the publication of this paper.

## References

- [1] Selvakumar, S., Manivasagan, R. and Chinnappan, K. (2013) Biodegradation and Decolourization of Textile Dye Wastewater Using *Ganoder malucidum*. *3 Biotech*, **3**, 71-79. <https://doi.org/10.1007/s13205-012-0073-5>
- [2] Pitre, S.P., Yoon, T.P. and Scakano, J.C. (2017) Titanium Dioxide Visible Light Photocatalysis: Surface Association Enables photocatalysis with Visible Light Irradiation. *Chemical Communications*, **53**, 4335-4338. <https://doi.org/10.1039/C7CC01952A>
- [3] Saravanan, R., Agarwal, S., Gupta, V.K., Khan, M.M., Gracia, F., Mosquera, E., Narayan, V. and Stephen, A. (2018) Line Defect Ce<sup>3+</sup> Induced Ag/CeO<sub>2</sub>/ZnO Nanostructure for Visible-Light Photocatalytic Activity. *Journal of Photochemistry and Photobiology A: Chemistry*, **353**, 499-506. <https://doi.org/10.1016/j.jphotochem.2017.12.011>
- [4] Fazal, A., Javed, I., Tariq, J., Noor, B., Qaisar, M. and Muhammad, I. (2016) Structural, Morphological, Raman, Optical, Magnetic, and Antibacterial Characteristics of CeO<sub>2</sub> Nanostructures. *International Journal of Minerals, Metallurgy, and Materials*, **23**, 102-108. <https://doi.org/10.1007/s12613-016-1216-1>
- [5] Nai, T., Liu, J.Y. and Shen, W.J. (2013) Tuning the Shape Ceria Nanomaterials for Catalytic Applications. *Chinese Journal of Catalysis*, **34**, 838-850. [https://doi.org/10.1016/S1872-2067\(12\)60573-7](https://doi.org/10.1016/S1872-2067(12)60573-7)
- [6] Thaís, M.N., Tuanny, S.F., Evelyn, C.C.D.S., Marcos, A.G. and Vanessa, B.M. (2017) An Investigation into an Alternative Photocatalyst Based on CeO<sub>2</sub>/Al<sub>2</sub>O<sub>3</sub> in Dye Degradation. *Environmental Technology & Innovation*, **8**, 349-359. <https://doi.org/10.1016/j.eti.2017.08.003>
- [7] Tan, J.P.Y., Tan, H.R., Boothroyd, C., Foot, Y.L., Het, C.B. and Lint, M. (2011) Three-Dimensional Structure of CeO<sub>2</sub> Nanocrystals. *Journal of Physical Chemistry C*, **115**, 3544-3551. <https://doi.org/10.1021/jp1122097>
- [8] Choi, J., Park, H. and Hoffmann, M.R. (2010) Effects of Single Metal-Ion Doping on the Visible-Light Photoreactivity of TiO<sub>2</sub>. *Journal of Physical Chemistry C*, **114**, 783-792. <https://doi.org/10.1021/jp908088x>
- [9] Machida, M., Kawada, T., Fujii, H. and Hinokuma, S. (2015) The Role of CeO<sub>2</sub> as a Gateway for Oxygen Storage over CeO<sub>2</sub>-Grafted Fe<sub>2</sub>O<sub>3</sub> Composite Materials. *Journal of Physical Chemistry C*, **119**, 24932-24941. <https://doi.org/10.1021/acs.jpcc.5b09876>
- [10] Tarak, M., Nidhi, K., Ritesh, M. and Kamal, K.P. (2016) Catalytic Steam Reforming

- of Model Oxygenates of Bio-Oil for Hydrogen Production Over La Modified Ni/CeO<sub>2</sub>-ZrO<sub>2</sub> Catalyst. *Topics in Catalysis*, **59**, 1343-1353. <https://doi.org/10.1007/s11244-016-0662-3>
- [11] Liu, W., Feng, L.J., Zhang, C., Yang, H.X., Guo, J.X., Liu, X.F., Zhang, X.Y. and Yang, Y.Z. (2013) A Facile Hydrothermal Synthesis of 3D Flowerlike CeO<sub>2</sub> via a Cerium Oxalate Precursor. *Journal of Materials Chemistry A*, **1**, 6942-6948. <https://doi.org/10.1039/c3ta10487g>
- [12] Román, R.L., Ignacio, E., Esaú, E., Rodrí, G.M., Silverio, M.L. and Abelardo, I.F.V. (2017) Al<sub>2</sub>O<sub>3</sub>-CeO<sub>2</sub> Sol-Gel Synthesis and Addition of Rh to Improve the Oxygen Mobility of Mixed Support. *Journal of Sol-Gel Science and Technology*, **81**, 214-219. <https://doi.org/10.1007/s10971-016-4184-z>
- [13] Sun, C.W., Xie, Z., Xia, C.R., Li, H. and Chen, L.Q. (2006) Investigations of Mesoporous CeO<sub>2</sub>-Ru as a Reforming Catalyst Layer for Solid Oxide Fuel Cells. *Electrochemistry Communications*, **8**, 833-838. <https://doi.org/10.1016/j.elecom.2006.03.018>
- [14] Jeong, M., Nunotani, N., Moriyama, N. and Imanaka, N. (2017) Introduction of NiO in Pt/CeO<sub>2</sub>-ZrO<sub>2</sub>/γ-Al<sub>2</sub>O<sub>3</sub> Catalysts for Removing Toluene in Indoor Air. *Materials Letters*, **208**, 43-45. <https://doi.org/10.1016/j.matlet.2017.05.048>
- [15] Liu, C.B., Sun, H., Qian, J.C., Chen, Z.G., Lv, Y.F., Chen, F., Lu, X.W. and Wu, Z.Y. (2017) Biotemplating Synthesis and Photocatalytic Activities of N-doped CeO<sub>2</sub> Microcapsule Tailored by Hemerocallis Pollen. *Advanced Powder Technology*, **28**, 2741-2746. <https://doi.org/10.1016/j.apt.2017.07.027>
- [16] Satyanarayana Reddy, A., Chen, C.Y., Chen, C.C., Chen, S.H., Lin, C.J., Lin, K.H., Chen, C.L. and Chang, S.C. (2010) Synthesis and Characterization of Fe/CeO<sub>2</sub> Catalysts: Epoxidation of Cyclohexene. *Journal of Molecular Catalysis A: Chemical*, **318**, 60-67. <https://doi.org/10.1016/j.molcata.2009.11.008>
- [17] Li, Y.F., He, Y.H., Liu, G.Q. and Zeng, L.W. (2018) Influence of La Precursors on Structure and Properties of CeO<sub>2</sub>-ZrO<sub>2</sub>-Al<sub>2</sub>O<sub>3</sub> Composite Oxides. *Transactions of Nonferrous Metals Society of China*, **28**, 739-747. [https://doi.org/10.1016/S1003-6326\(18\)64706-5](https://doi.org/10.1016/S1003-6326(18)64706-5)
- [18] Yu, X.X., Dong, Z.F., Yang, X., Dong, B. and Wu, Y. (2017) Facile Synthesis of ZnO Nanoparticles for the Photocatalytic Degradation of Methylene Blue. *Journal of Sol-Gel Science and Technology*, **82**, 167-176. <https://doi.org/10.1007/s10971-016-4297-4>
- [19] Zhang, C., Zhang, X.Y., Wang, Y.C., Xie, S.L., Liu, Y., Lu, X.H. and Tong, Y.X. (2014) Facile Electrochemical Synthesis of CeO<sub>2</sub> Hierarchical Nanorods and Nanowires with Excellent Photocatalytic Activities. *New Journal of Chemistry*, **38**, 2581. <https://doi.org/10.1039/C4NJ00214H>
- [20] Liu, Y. and Sun, D.Z. (2007) Effect of CeO<sub>2</sub> Doping on Catalytic Activity of Fe<sub>2</sub>O<sub>3</sub>/γ-Al<sub>2</sub>O<sub>3</sub> Catalyst for Catalytic Wet Peroxide Oxidation of Azo Dyes. *Journal of Hazardous Materials*, **43**, 448-454. <https://doi.org/10.1016/j.jhazmat.2006.09.043>
- [21] Lamdab, U., Wetchakun, K., Phanichphanrs, S., Kangwansuamonkon, W. and Wetchakun, N. (2015) Highly Efficient Visible Light-Induced Photocatalytic Degradation of Methylene Blue over InVO<sub>4</sub>/BiVO<sub>4</sub> Composite Photocatalyst. *Journal of Materials Science*, **50**, 5788-5798. <https://doi.org/10.1007/s10853-015-9126-6>
- [22] Choudhury, B., Chetri, P. and Choudury, A. (2014) Oxygen Defects and Formation of Ce<sup>3+</sup> Affecting the Photocatalytic Performance of CeO<sub>2</sub> Nanoparticles. *RSC Advances*, **4**, 4663-4671. <https://doi.org/10.1039/C3RA44603D>
- [23] Chen, H., Saysri, A., Adaot, A. and Larachi, F. (2001) Composition-Activity Effects

- 
- of Mn-Ce-O Composites on Phenol Catalytic Wet Oxidation. *Applied Catalysis B: Environmental*, **32**, 195-204. [https://doi.org/10.1016/S0926-3373\(01\)00136-9](https://doi.org/10.1016/S0926-3373(01)00136-9)
- [24] Neri, G., Pistone, A., Milone, C. and Galvagno, S. (2002) Wet Air Oxidation of Pcoumaric Acid over Promoted Ceria Catalysts. *Applied Catalysis B: Environmental*, **38**, 321-329. [https://doi.org/10.1016/S0926-3373\(02\)00061-9](https://doi.org/10.1016/S0926-3373(02)00061-9)
- [25] Reina, T.R., Ivanova, S., Centenom, A. and Odriozola, J.A. (2015) Catalytic Screening of Au/CeO<sub>2</sub>-MO<sub>x</sub>/Al<sub>2</sub>O<sub>3</sub> Catalysts (M<sup>1/4</sup> La, Ni, Cu, Fe, Cr, Y) in the CO-PrOx Reaction. *International Journal of Hydrogen Energy*, **40**, 1782-1788. <https://doi.org/10.1016/j.ijhydene.2014.11.141>